Physics principles in radiometric infrared imaging of clouds in the atmosphere

2013 Eur. J. Phys. 34 S111

(http://iopscience.iop.org/0143-0807/34/6/S111)

IOP PUBLISHING EUROPEAN JOURNAL OF PHYSICS

Eur. J. Phys. **34** (2013) S111–S121 doi:10.1088/0143-0807/34/6/S111

Physics principles in radiometric infrared imaging of clouds in the atmosphere

Joseph A Shaw[1] **and Paul W Nugent**

Electrical and Computer Engineering Department, Montana State University, Bozeman,
MT 59717, USA

E-mail: jshaw@montana.edu

Received 12 June 2013, in final form 8 July 2013
Published 22 October 2013
Online at stacks.iop.org/EJP/34/S111

Abstract

Imaging the atmosphere with a thermal infrared camera can yield a rich variety of information, ranging from the water-vapour content to the spatial distribution of clouds. Such remote sensing measurements are being used to study climate and to characterize ground-station sites for Earth–space optical communications. The key to turning interesting but qualitative images into the highly accurate quantitative images required for this type of research is careful radiometric calibration. This is especially true when using uncooled microbolometer cameras, which are becoming widely available at relatively low cost. When such cameras are calibrated properly, their images illustrate a variety of important basic principles of optics and atmospheric physics related to thermal emission and absorption by atmospheric gases and clouds.

(Some figures may appear in colour only in the online journal)

1. Introduction

Observing the atmosphere is a rich source of lessons in optics and atmospheric physics. The scattering of sunlight by tiny gas molecules creates a deep blue clear sky, while the same scattering process with longer paths at sunrise or sunset removes the blue skylight to create the warm orange and red colours that are best seen reflected by the much larger water droplets or ice crystals of clouds; with shorter atmospheric paths, the scattering by larger water or ice particles creates white or grey clouds [1]. The Sun or Moon, observed through optically thin clouds, can be surrounded by colourful diffraction rings (called the corona), whose sizes can be related to the size of the cloud's water droplets [1, 2] or tiny ice crystals [3]. In deep twilight, a combination of high-altitude particle scattering and gaseous absorption can turn the sky a subtle but striking purple colour [1, 4]. In the midst of rain showers, the even-larger rain drops

---

[1] Author to whom any correspondence should be addressed.

0143-0807/13/060111+11$33.00

refract and reflect light to disperse the colours into a rainbow [1, 5, 6]. Ice crystals in the air can refract and reflect light to create spectacular halo patterns or simple parhelia (or 'sundogs') [1, 7–10]. These interactions of visible light with objects of such a wide range of sizes—from molecules to ice crystals—provides a continuum of lessons in optics and atmospheric physics, vividly illustrating the basic principles of scattering, diffraction, absorption, refraction and reflection.

There are similarly rich lessons in optics and atmospheric physics from thermal infrared (IR) observations, but in this case the concepts most readily illustrated are absorption and emission. Because of limited experience in observing thermal IR phenomena, many people find these lessons more difficult to conceptualize. Nevertheless, the rapidly increasing technological capabilities and decreasing costs of thermal IR cameras are combining to make such observations more practical. Some excellent applications of thermal IR cameras for teaching university-level physics were presented recently by Möllmann and Vollmer [11], ranging from visualizing electromagnetic modes in a microwave oven and transient heat transfer when a tennis ball strikes the floor, to noninvasively determining the internal structural pattern of plaster walls. Additional examples were described along with an excellent discussion of the technology and physics of thermal imaging by Vollmer and Möllmann [12]. In a similar spirit, this paper illustrates some of the physics principles that become apparent when an IR camera is used to observe the atmosphere.

2. Radiometric imaging with uncooled infrared cameras

The increasing availability of thermal cameras arises primarily because of the development of uncooled IR imaging systems that do not require cryogenically cooled detectors [13]. These systems typically rely on microbolometer detector arrays that produce qualitatively useful images, but are rather difficult to calibrate for quantitative radiometric measurements. Primary sources of this difficulty include an inherently non-uniform pixel-to-pixel response and a high sensitivity to changes in the camera's focal-plane-array temperature. These challenges become even more significant when the imaging system is pointed at an object with low thermal emission, such as the atmosphere.

By acquiring images of a large-area blackbody calibration source immediately before and after an atmospheric image, it is possible to obtain radiometric images in which the digital number of each pixel is converted to a quantity such as radiance in W $(\mathrm{m}^2\ \mathrm{sr})^{-1}$ or brightness temperature in K [14–17]. However, if such a large and expensive source is not available or not desired in the field, the methods we described recently are capable of stabilizing the self-temperature response of microbolometer cameras, thereby allowing them to maintain calibration even when operated outdoors in a changing environment [17].

These calibration methods were developed to enable high-accuracy, calibrated imaging of the long-wave IR emission from the atmosphere for measuring spatial and temporal cloud patterns [14, 15, 18, 19], but they also have enabled diverse remote sensing applications that include locating underground CO_2 gas leaks [20] and monitoring the population of bee hives [21]. Uncooled imagers are desirable in this kind of research because they can be used in long-term deployments at remote field sites. Two examples of radiometric images obtained from long-wave IR microbolometer cameras in the 8–14 μm spectral band are shown in figure 1. The first example (figure 1(a)) is an image of a wolf at night, calibrated to show the brightness temperature T_b in degrees C. At the time this image was acquired, the wolf's body was in thermal equilibrium with its surroundings, so the only observable warm spots in the image were the wolf's eyes, face and forelegs. The second example (figure 1(b)) is an image of a

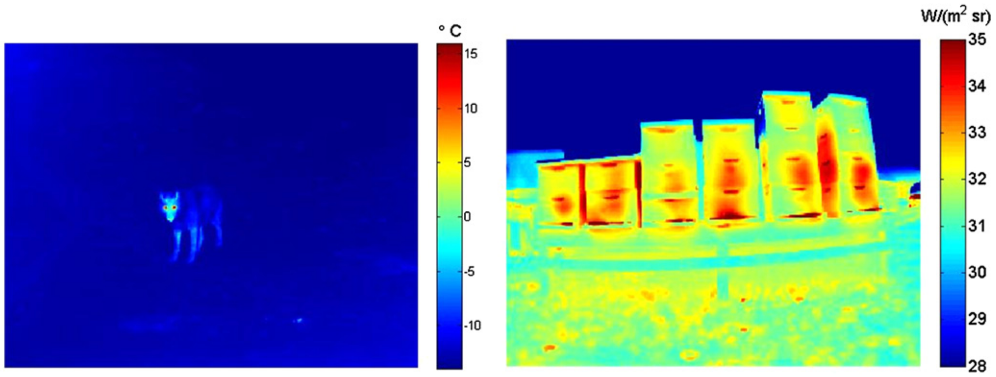

Figure 1. Radiometric images from a long-wave infrared microbolometer camera with wavelength coverage of approximately 8–14 μm. (a) A temperature image of a wolf observed at night, assuming emissivity = 1 (the colour indicates the temperature in °C); (b) a radiance image of beehives (the colour indicates the radiance in W m^{-2} sr^{-1}), used to estimate hive populations [21].

bee hive, calibrated in radiance units of W (m^2 sr)$^{-1}$. This sort of imagery has been used to estimate the population and robustness of bee hives [21].

Radiance and brightness temperature are related through Planck's radiation law, which in the form shown in equation (1) expresses the spectral radiance [Watts per (area × solid angle × wavelength interval)] emitted by an object as a function of temperature and wavelength.

$$L^{bb}(\lambda,T) = \frac{2hc^2}{\lambda^5}\frac{1}{\mathrm{e}^{\frac{hc}{\lambda k T_b}} - 1}. \qquad (1)$$

In this equation, h is Planck's constant (6.626×10^{-34} J s), k is Boltzmann's constant (1.381×10^{-23} J K^{-1}), c is the speed of light in a vacuum (2.998×10^{8} m s^{-1}), λ is the electromagnetic wavelength and T is the temperature of the emitting object. More generally, this equation is multiplied by a wavelength-dependent factor called the emissivity, which varies between 0 for a non-radiating object (a perfect mirror) and 1 for an ideal blackbody (note that the brightness temperature is less than the physical temperature unless the emissivity = 1, and in the case of the wolf image shown in figure 1 the emissivity has been assumed to be 1). Figure 2 is a plot of blackbody spectral radiance versus wavelength for a blackbody at a temperature of 288 K, typical of the temperature of air near the Earth's surface. The peak near 10 μm wavelength would shift to longer wavelengths for colder temperatures and would shift to shorter wavelengths for higher temperatures.

3. Thermal emission from the atmosphere

A somewhat more abstract concept than emission from solid objects is that of thermal emission from the gas molecules of the atmosphere. However, vibrations and rotations of these molecules constitute electrical charges in motion, and therefore produce electromagnetic radiation—in this case in the form of thermal IR emission. Because thermal equilibrium requires the rate of emission to equal the rate of absorption (Kirchhoff's radiation law), the atmosphere emits radiation most readily at the same wavelengths that it absorbs effectively. Consequently, we begin this discussion with an examination of atmospheric transmittance, which is plotted as a function of wavelength in figure 3. Most of the spectral structure is a result of molecular absorption by atmospheric gases (primarily trace gases such as water vapour, ozone and carbon

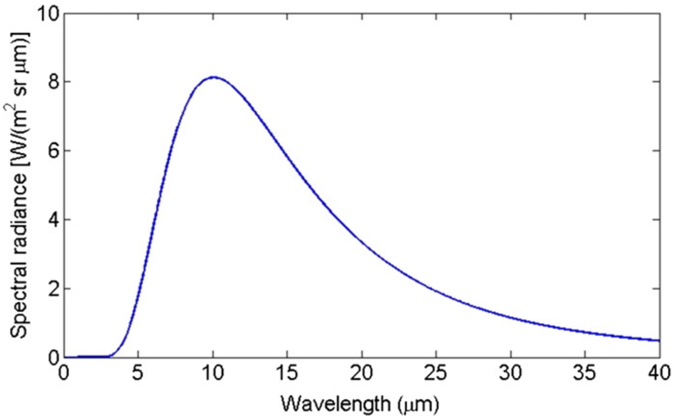

Figure 2. Plot of blackbody spectral radiance (equation (1)) versus wavelength for a 288 K blackbody.

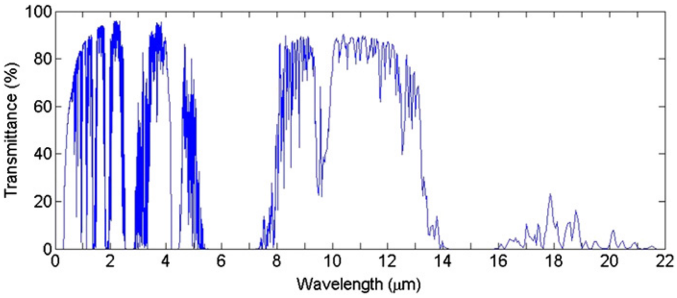

Figure 3. Atmospheric transmittance versus wavelength, calculated with Modtran5 for a zenith path from sea level to space through a 1976 US Standard Atmosphere model.

dioxide, which constitute less than 1% of the atmosphere). One notable exception is the roll-off of transmittance at wavelengths below about 2 μm, which is caused by a combination of molecular scattering (Rayleigh scattering, varying as wavelength^{-4}) and strong ozone absorption below 0.35 μm. Note also that this spectrum was calculated for very clean air, using the Modtran Rural aerosol model with 23 km visibility. In a more urban environment there would be significantly more aerosols, which would result in scattering that would reduce the visible transmittance well below what is shown in figure 3. In fact, one effect of abundant aerosol scattering in dry air is to reduce the visible atmospheric transmittance notably below the IR transmittance in the 8–14 μm spectral region.

Spectral regions with high transmission are called 'atmospheric windows', which include the visible (~0.4–0.7 μm), short-wave infrared (SWIR ~1–2 μm), mid-wave infrared (MWIR ~3–5 μm), and long-wave infrared (LWIR ~8–14 μm). The MWIR window is interrupted by carbon dioxide absorption centred at 4.3 μm and the LWIR window has ozone absorption centred at 9.6 μm. The overall envelope of the LWIR transmission window is governed by the amount of water vapour in the atmosphere at any given time and place.

Water-vapour content is also a fundamental parameter in determining the amount of emission in the LWIR window, as shown in figure 4. This is a plot of atmospheric radiance (solid blue curve) and 288 K blackbody radiance (dashed red line), emitted as a function of wavelength in the thermal IR region. The atmospheric emission is calculated with Modtran5 for

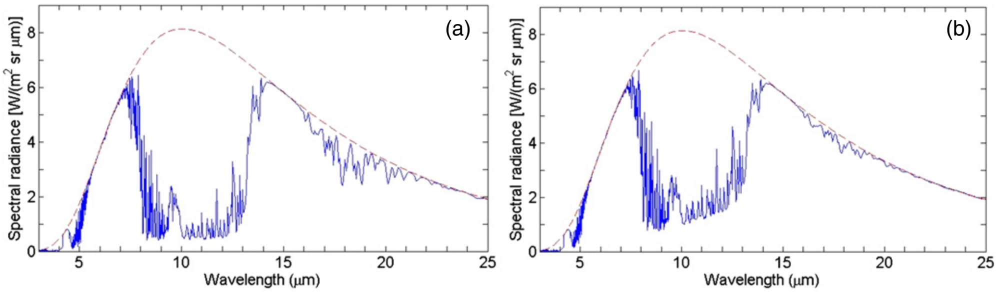

Figure 4. Atmospheric emitted radiance (solid blue line) and 288 K blackbody radiance (dashed red line) plotted versus wavelength for (a) 1 cm PWV and (b) 2 cm PWV. Both spectra were calculated with Modtran5 for the conditions of figure 3.

two different values of integrated water-vapour content in the 1976 US Standard Atmosphere model. The blue curve in figure 4(a) is for 1 cm of ‘precipitable water vapour’ (PWV, the thickness of liquid water that would result from compressing all the water vapour in the atmosphere until it precipitated as liquid), while the blue curve in figure 4(b) is for 2 cm of PWV. For reference, 1 cm is a typical PWV value during the dry winter months in much of Europe and the central US, while 2 cm is a typical summertime value in these same locations. Very low humidity levels would be typified by a PWV value of 0.5 cm (sometimes much less) during the dry season in the deserts of the southwest US, Northern Africa and Asia (e.g. Mongolia), or even the high Arctic and Antarctic regions. Very high humidity would be typified by a PWV value in the range of 3–5 cm during the wet season in locations such as southeast Asia and the tropics. A useful tool for exploring the PWV at many locations around the world is the Aerosol Robotic Network (AERONET), a NASA network of stations that measure atmospheric aerosol properties and PWV with sun-viewing solar radiometers [22].

Careful examination of figure 4 reveals that atmospheric emission resembles the transmission spectrum of figure 3 flipped upside down and spectrally weighted by a blackbody curve at the near-surface air temperature of 288 K (see figure 2). This results in a high emission relative to the blackbody envelope at wavelengths with low transmittance. In keeping with this behaviour, the two emission spectra with different values of PWV follow essentially the same blackbody curve at wavelengths above 22 μm and between 6–8 μm, because of high water-vapour absorption (in fact, atmospheric transmittance is not shown above 22 μm in figure 3 because it is essentially zero). The same behaviour is observed at 14–16 μm because of carbon dioxide absorption, and to a lesser degree at 16–22 μm because of water-vapour absorption.

We can solve the Planck blackbody function (equation (1)) for temperature at each wavelength to convert the atmospheric radiance spectra in figure 4 into the brightness temperature (T_b) spectra in figure 5. Since the air temperature generally becomes colder with altitude in the troposphere, an IR imager looking up from the ground will see the warmest air nearest the imager and colder air at higher altitudes. Consequently, figures 4 and 5 generally follow a blackbody curve for a near-surface air temperature near 288 K at wavelengths with high absorption. Deviations below this envelope occur at wavelengths where the transmission is sufficiently high to allow the imager to observe emission from colder air at higher altitudes. In fact, at the more highly transmitting wavelengths, the imager observes integrated emission from a range of altitudes and therefore a range of temperatures, so the regions of lower emission match a blackbody curve for a temperature that is a weighted integral over the observed altitude range. Note that the minimum T_b occurs in the LWIR window in the approximate wavelength

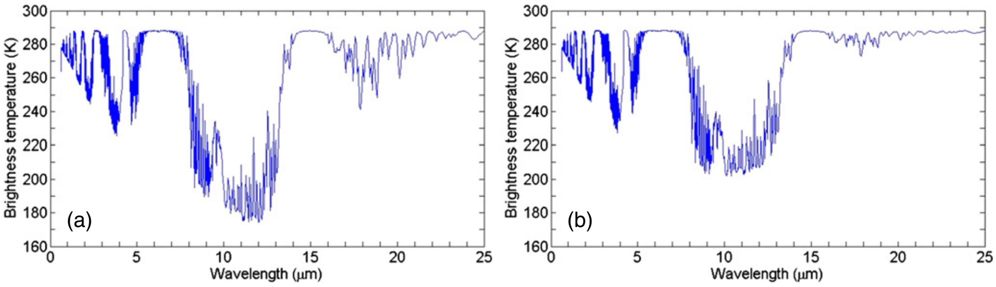

Figure 5. Atmospheric brightness temperature spectra corresponding to the emission spectra in figure 4: (a) PWV = 1 cm, (b) PWV = 2 cm.

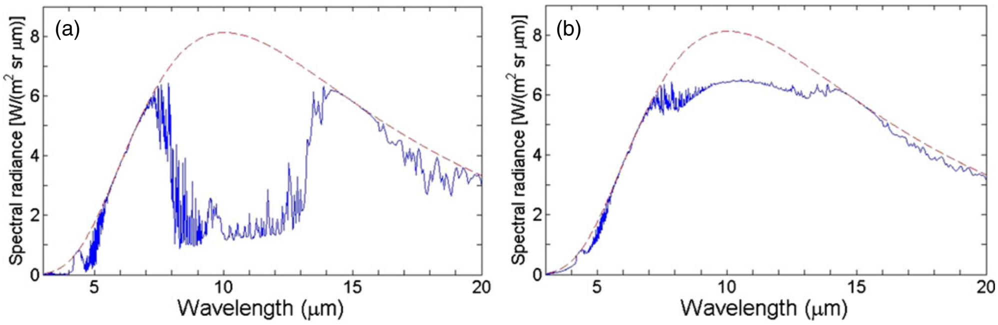

Figure 6. Emission spectra of clouds observed at the zenith from the ground, modelled with Modtran5 for the 1976 US Standard Atmosphere: (a) cirrus with 10 km base altitude, 2 km thickness, and 0.28 extinction; and (b) optically opaque altostratus cloud with a 2.4 km base and 3.0 km top.

range of 8–14 μm. It is also important to note the large difference in radiance or T_b that arises because of the differing PWV values (1 cm for figure 5(a) and 2 cm for figure 5(b)). This shows clearly that the LWIR-window atmospheric emission varies primarily with changing PWV.

For reference, if we consider an IR imager located on a satellite looking down, it would observe spectra that are the approximate inverses of figures 4 and 5. The highest radiance or T_b would be emitted by the underlying surface, which would be visible to the satellite-based imager only in the window regions. In spectral regions with high absorption, the imager would see emission from cold air at high altitudes.

4. Infrared cloud imaging

Clouds also emit thermal radiation, and except for thin cirrus they emit a nearly ideal blackbody spectrum corresponding to the altitude-dependent cloud temperature and cloud emissivity, which is 1 for clouds with at least 0.1 mm of integrated liquid [23] and is usually less than 1 for ice clouds with an ice water path less than 0.1 mm [24]. Optically thick cloud emission is therefore similar to a blackbody curve at or near the temperature of the cloud (i.e., the air temperature at the cloud-base altitude). This is illustrated in figure 6, which shows emission spectra from (a) a 2 km thick cirrus cloud at 10 km with an integrated extinction of 0.28 at 0.55 μm wavelength and a mean temperature of 216.8 K, and (b) an optically opaque, 0.6 km

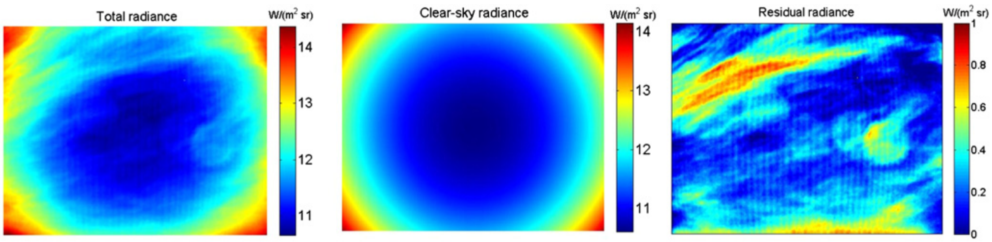

(a) (b) (c)

Figure 7. LWIR images of down-welling emission from the atmosphere with thin clouds above Barrow, Alaska at 1657 UTC on 19 July 2012: (a) total radiance (clear sky and clouds); (b) clear-sky radiance calculated for PWV = 1.8 cm and near-surface air temperature = 1.1 °C; (c) residual radiance (a–b) showing which pixels observe radiance significantly higher than the clear-sky value, indicating the presence of clouds.

thick altostratus cloud at 2.4 km with a mean temperature of 271.6 K. Figures 6(a) and (b) both show cloud emission as a solid blue curve and (for reference) 288 K blackbody emission as a dashed red line.

It is straightforward to infer from figure 6 that the altostratus cloud emits as a blackbody with a temperature slightly lower than the near-surface air (the cloud emission has a lower-amplitude peak at a slightly longer wavelength than the blackbody envelope of the near-surface air). However, the cirrus cloud spectrum is different from a blackbody because it is not optically opaque. Furthermore, the cirrus emission is similar to the emission spectrum of the clear atmosphere with increased water vapour (compare figure 6(a) with figure 4(b)). From these observations we can state three conclusions: (1) clouds are readily observed in the LWIR-window region; (2) cirrus cloud emission in the LWIR window closely resembles clear-sky emission, so thin cirrus can be quite difficult to distinguish from the clear sky, especially at higher humidity levels; and (3) optically thick clouds, which occur typically at lower, warmer altitudes, are easy to differentiate from clear-sky emission.

In the infrared cloud imager (ICI) method, we apply a radiometric calibration to the IR images and carefully compensate for the estimated clear-sky emission so that thin cirrus clouds can be detected in the presence of variable atmospheric conditions [14, 15, 18, 19]. This procedure requires integrating the cloud spectral radiance (figure 6) over the spectral response function of the IR camera to determine the observed broadband radiance. For the FLIR Photon 320 camera used to acquire the data shown here, the spectral response function is a Gaussian-like curve with 50%-sensitivity points at wavelengths of approximately 8.4 μm and 13.8 μm (typical of many LWIR cameras). Figure 6 shows that the bulk of the camera's signal is from within the atmospheric window; however, because the camera's response extends into the water-vapour emission below 8 μm and the carbon dioxide emission above 14 μm, the observed radiance is a stronger function of air temperature than it would be with a narrower bandwidth.

The following figures are example sky images obtained in Barrow, Alaska with a zenith-pointing ICI system using a FLIR Photon 320 camera with 324 × 256 pixels and a custom wide-angle lens with a 110° diagonal field of view. Figure 7(a) shows total band-averaged sky radiance (W (m^2 sr)$^{-1}$) measured at 1657 UTC on 19 July 2012. In other words, this is a measurement of the spatial distribution of band-average radiance emitted towards the ground by the clear atmosphere and clouds. Figure 7(b) is the clear-sky emission for the same camera bandwidth, calculated from the measured PWV (1.83 cm) and near-surface air temperature (1.11 °C). Figure 7(c) is the difference between the total and clear-sky radiance, which we call the residual radiance. This should be zero (within the calibration uncertainty) at cloud-free

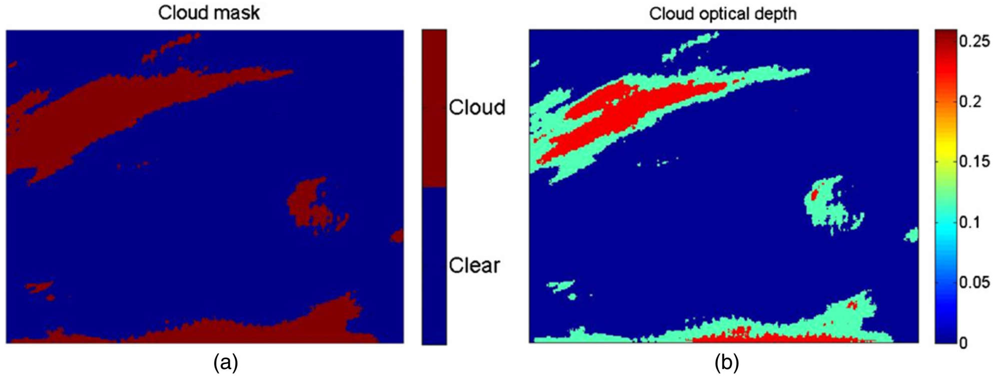

(a) (b)

Figure 8. Cloud products derived from the residual radiance in figure 7(c): (a) cloud presence (red is cloud and blue is clear); (b) cloud optical depth.

pixels. Because the colour scale is compressed to cover such a small radiance range (0–1 W $(m^2\ sr)^{-1}$) and because these clouds are quite thin, this particular image shows a significant amount of spatial noise and image artefacts; for example, there are vertical stripes caused by the micro-groove structure of the blackbody calibration source [16] and several circular patterns which are likely to have been caused by dust particles on the sensor or perhaps the lens. However, additional image processing can remove much of this variability. Once this processing is complete, the value of residual radiance is used to identify the presence of clouds and also to estimate the visible-wavelength cloud optical depth (OD), a dimensionless number describing the path-integrated extinction through the cloud [25]. Therefore, IR cameras are not only capable of mapping out regions of the sky that contain clouds, but also of mapping out the spatial distribution of cloud radiance, temperature and OD (similar IR imagers have been used by Smith and Toumi to determine cloud radiative forcing [26]). Example cloud products are shown in figure 8(a), a cloud map that indicates which pixels contain clouds and which do not, and figure 8(b) shows a cloud OD map that adds information about the spatial distribution of the cloud optical characteristics.

The cloud OD can be estimated from ICI images up to a value of approximately 4. Clouds emit as blackbodies at larger OD values, meaning the ICI measurements of such clouds can only tell us that the cloud OD is equal to or greater than this value. The method of estimating cloud OD from ICI images is to first estimate the LWIR emissivity from the cloud radiance, which requires knowing or assuming the cloud altitude and temperature [25]. The LWIR emissivity of a thin cloud can be approximated within narrow spectral bands as $1–\exp(-0.79\tau)$, where τ is the visible cloud OD [27, 28]. (This is a model for narrow 'micro-window' spectral bands, and we are studying how it might need to be modified for optimal application to wider bandwidths.) Finally, the LWIR cloud OD is estimated as half the visible cloud OD [29, 30]. This entire procedure requires the cloud height, which can be assumed or measured with a LIDAR instrument.

The measurement leading to figures 7 and 8 was for a PWV value (1.8 cm) that is surprisingly high in the Arctic, presumably because of moisture arising from the nearby ocean. The relatively high PWV provides an excellent demonstration of how the clear-sky radiance can be the largest radiance component in a LWIR sky image. Notice, for example, that very thin clouds at the zenith (i.e., the centre of figure 7(a)) emit only approximately 1 W $(m^2\ sr)^{-1}$ more than the nearby clear sky. An observer can discern that clouds are present in the total radiance image of figure 7(a), but the overall spatial pattern in this image is dominated by the variation of atmospheric path length with angle from the zenith. Without accurate compensation of the

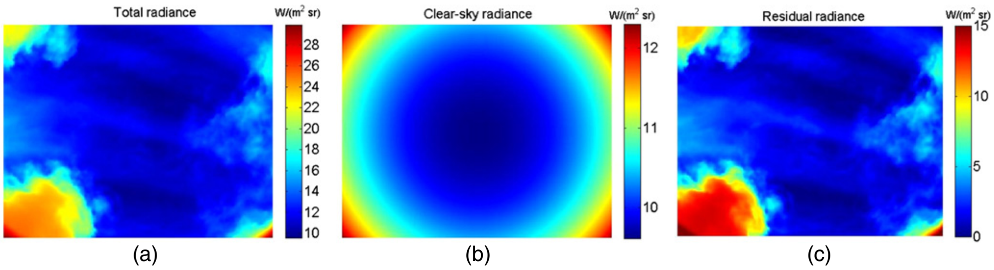

Figure 9. LWIR images of down-welling emission from a partly cloudy atmosphere above Barrow, Alaska at 1526 UTC on 21 July 2012: (a) total radiance (clear sky and clouds); (b) clear-sky radiance for PWV = 1.1 cm and near-surface air temperature = −1.1 °C; (c) residual radiance (a–b) showing which pixels observe radiance significantly higher than the clear-sky value, indicating the presence of clouds.

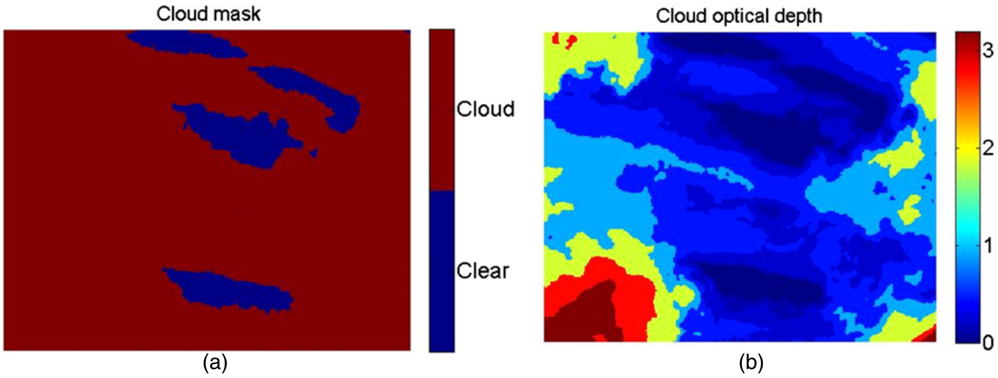

Figure 10. Cloud products derived from the residual radiance in figure 9(c): (a) cloud presence (red is cloud and blue is clear sky); (b) cloud optical depth.

angle-dependent clear-sky emission shown in figure 7(b), it would be difficult or impossible to properly identify cloudy and clear pixels (such as figures 8(a) and (b)). Even with careful removal of the clear-sky emission, the thin clouds in this example exhibit a very small signal.

Figure 9 shows an example with thicker clouds that exhibit notably higher emission than those in figure 7. This is a measurement from Barrow, Alaska, at 1526 UTC on 21 July 2012, with PWV of 1.1 cm and an air temperature of −1.1 °C. The lower PWV value (with comparable air temperature) leads to a lower clear-sky radiance compared with figure 7(b), and the optically thicker clouds generate a much larger total radiance and residual radiance signal relative to figures 7(a) and (c). The corresponding cloud-mask and cloud OD images are shown in figure 10. The added information content is apparent in the cloud OD image of figure 10(b) relative to the simple cloud-mask image of figure 10(a).

The inevitable questions about minimum detectable signal or minimum detectable cloud OD are difficult to answer precisely, primarily because they depend very strongly on the atmospheric conditions and the amount and type of processing performed on the images. With our custom calibration methods applied, uncooled microbolometer long-wave IR cameras usually have a noise level corresponding to a blackbody temperature near −60 °C. A more common figure of merit for thermal imagers is the noise-equivalent temperature difference (NETD), which is the (usually temporal) temperature change that produces a signal change equal to the noise, resulting in a signal-to-noise ratio of 1. This type of camera typically has NETD of approximately 30–50 mK with an F/1 lens. For our standard ICI instruments, clouds can be detected down to an OD of approximately 0.1 without extra thin-cloud processing enhancements.

5. Conclusion

The increasing availability and quality of infrared imagers is making it more practical to use them for teaching about physics in the atmosphere. Relatively low-cost infrared imagers using microbolometer detectors can be calibrated to accurately measure sky emission, with sufficient care. The principles outlined in this paper can be used to interpret such images quantitatively or qualitatively, especially relating to the atmospheric water-vapour content, cloud altitude, cloud temperature and cloud optical depth. At any one angle, the clear-sky emission increases primarily with water-vapour content, but also with air temperature. The clear-sky emission increases steadily at angles away from the zenith direction, producing a circular pattern centred on the zenith. Removing the clear-sky emission produces a residual radiance pattern that indicates the spatial pattern of clouds, if any. The value of this residual can be used not only to identify the presence of clouds, but also to estimate the value of the optical depth of the clouds.

Acknowledgment

This research was performed with funding from the US National Science Foundation through Award ARC-1108427.

References

[1] Lynch D K and Livingston W 2001 *Color and Light in Nature* (New York: Cambridge University Press)
[2] Gedzelman S D 2008 Simulating halos and coronas in their atmospheric environment *Appl. Opt.* **47** H157–66
[3] Shaw J A and Pust N J 2011 Icy wave-cloud lunar corona and cirrus iridescence *Appl. Opt.* **50** F6–11
[4] Lee R L and Hernandez-Andres J 2003 Measuring and modeling twilight's purple light *Appl. Opt.* **42** 445–57
[5] Lee R L and Fraser A B 2001 *The Rainbow Bridge: Rainbows in Art, Myth, and Science* (University Park, PA: Pennsylvania State University Press)
[6] Laven P 2003 Simulation of rainbows, coronas and glories by use of Mie theory *Appl. Opt.* **42** 436–44
[7] Tape W 1994 *Atmospheric Halos* (Washington, DC: American Geophysical Union)
[8] Tape W and Moilanen J 2006 *Atmospheric Halos and the Search for Angle x* (Washington, DC: American Geophysical Union)
[9] Vollmer M and Greenler R G 2003 Halo and mirage demonstrations in atmospheric optics *Appl. Opt.* **42** 394–8
[10] Greenler R G, Mueller J R, Hahn W and Mallmann A James 1979 The 46° halo and its arcs *Science* **206** 643–9
[11] Möllmann K-P and Vollmer M 2007 Infrared thermal imaging as a tool in university physics education *Eur. J. Phys.* **28** S37–50
[12] Vollmer M and Möllmann K-P 2010 *Infrared Thermal Imaging: Fundamentals, Research and Applications* (Weinheim: Wiley)
[13] Kruse P W 2001 *Uncooled Thermal Imaging Arrays, Systems, and Applications* (Bellingham, WA: SPIE Optical Engineering Press)
[14] Shaw J A, Nugent P W, Pust N J, Thurairajah B and Mizutani K 2005 Radiometric cloud imaging with an uncooled microbolometer thermal infrared camera *Opt. Express* **13** 5807–17
[15] Thurairaijah B and Shaw J A 2005 Cloud statistics measured with the infrared cloud imager *IEEE Trans. Geosci. Remote Sens.* **43** 2000–7
[16] Nugent P W and Shaw J A 2009 Large-area blackbody emissivity variation with observation angle *Proc. SPIE* **7300** 73000Y
[17] Nugent P W, Shaw J A and Pust N J 2013 Correcting for focal plane array temperature dependence in microbolometer infrared cameras lacking thermal stabilization *Opt. Eng.* **52** 061304
[18] Nugent P W, Shaw J A and Piazzolla S 2009 Infrared cloud imaging in support of Earth–space optical communication *Opt. Express.* **17** 7862–72

[19] Nugent P W, Shaw J A and Piazzolla S 2013 Infrared cloud imager development for atmospheric optical communication characterization, and measurements at the JPL table mountain facility *IPN Progress Report 42-192* (Pasadena, CA: Jet Propulsion Laboratory) http://tmo.jpl.nasa.gov/progress_report/42-192/192C.pdf (accessed 6 June 2013)

[20] Johnson J E, Shaw J A, Lawrence R, Nugent P W, Dobeck L M and Spangler L H 2012 Long-wave infrared imaging of vegetation for detecting leaking CO_2 gas *J. Appl. Remote Sens.* **6** 063612

[21] Shaw J A, Nugent P W, Johnson J, Bromenshenk J J, Henderson C B and Debnam S 2011 Long-wave infrared imaging for non-invasive beehive population assessment *Opt. Express* **19** 399–408

[22] NASA Goddard Space Flight Center Aerosol Robotic Network http://aeronet.gsfc.nasa.gov (accessed 6 June 2013)

[23] Shaw J A and Fedor L S 1993 Improved calibration of infrared radiometers for cloud temperature remote sensing *Opt. Eng.* **32** 1002–10

[24] Ebert E E and Curry J A 1992 A parameterization of ice cloud optical properties for climate models *J. Geophys. Res.* **97** 3831–6

[25] Shaw J A, Nugent P W, Pust N J, Redman B J and Piazzolla S 2012 Cloud optical depth measured with ground-based, uncooled infrared imagers *Proc. SPIE* **8523** 85231D

[26] Smith S and Toumi R 2008 Direct observation of cloud forcing by ground-based thermal imaging *Geophys. Res. Lett.* **35** L07814

[27] Sassen K and Mace G G 2002 *Ground-based remote sensing of cirrus clouds Cirrus* ed D K Lynch, K Sassen, D O'C Starr and G Stephens (New York: Oxford University Press) pp 168–209

[28] Fu Q and Liou K N 1993 Parameterization of the radiative properties of cirrus clouds *J. Atmos. Sci.* **50** 2008–25

[29] DeSlover D H, Smith W L, Piironen P K and Eloranta E W 1999 A methodology for measuring cirrus cloud visible-to-infrared spectral optical depth ratios *J. Atmos. Ocean. Technol.* **16** 251–62

[30] Platt C M R, Scott J C and Dilley A C 1987 Remote sounding of high clouds: part VI. Optical properties of midlatitude and tropical cirrus *J. Atmos. Sci.* **44** 729–47